Evolution of mechanical and rockburst parameters of gypsum-like rock under fatigue stress disturbance

Rock Mechanics Bulletin 4 (2025) 100171

Contents lists available at ScienceDirect

Rock Mechanics Bulletin

journal homepage: www.keaipublishing.com/en/journals/rock-mechanics-bulletin

Full Length Article

Evolution of mechanical and rockburst parameters of gypsum-like rock under fatigue stress disturbance

Chongyang Wang [a,b,c], Sijiang Wei [c], Dongming Zhang [a,*], Beichen Yu [a], Yisha Pan [d], Xunjian Hu [b,e]

[a] State Key Laboratory of Coal Mine Disaster Dynamics and Control, Chongqing University, Chongqing, 400030, China
[b] Department of Structural, Geotechnical and Building Engineering, Politecnico di Torino, Turin, 10138, Italy
[c] School of Energy Science and Engineering, Henan Polytechnic University, Jiaozuo, 454000, China
[d] School of Surveying, Mapping and Land Information Engineering, Henan Polytechnic University, Jiaozuo, 454000, China
[e] Research Center of Coastal and Urban Geotechnical Engineering, Zhejiang University, Hangzhou, 310058, China

ARTICLE INFO

Keywords:
Gypsum-like rock
Fatigue loading
Model building
Complex plane analysis
Neural network analysis

ABSTRACT

To investigate the deterioration of mechanical properties in engineering rock masses subjected to fatigue stress, this study conducted laboratory tests, theoretical analysis, and model building to analyze the evolution of mechanical and rockburst characteristics in gypsum-like rock before and after fatigue loading. The results showed that the effects of cyclic stress and loading frequency on fatigue damage characteristics of the samples are interrelated. The effect of fatigue cyclic stress on the mechanical parameters and rockburst parameters of the samples after fatigue loading is relatively straightforward, while the impact of frequency on the mechanical properties of samples after fatigue loading is more complex. The impact of frequency on mechanical properties and rockburst parameters varies distinctly under different cyclic stress conditions. A deterioration index model ($\lambda = p + jq$) was established for the samples after fatigue loading, and the real part, imaginary part, and $|\lambda|$ of the model were calculated to plot the function in the complex plane. This model provided insight into the evolution of mechanical properties and rockburst characteristics in gypsum-like rock before and after fatigue loading with different stress levels and frequencies. By examining the λ curve's position within the complex plane, the overall variation in mechanical properties was assessed. Finally, neural network methods were employed to extend and test the complex plane model, expanding the input factors from discrete data points to continuous definition fields on the number line, thereby increasing the model's practicality and applicability.

Variable annotations

Variable	Annotation	Variable	Annotation
σ_c	Uniaxial compressive strength before fatigue loading (MPa)	f	Loading frequency (Hz)
A	Loading amplitude ($n\cdot\sigma_c$)	C	The central value of fatigue loading ($n\cdot\sigma_c$)
σ_{cf}	Uniaxial compressive strength after fatigue loading (MPa)	a, b, l, m, f	Fitting parameters of Parabola^{2D} function
ε_c	Peak strain (10^{-3})	λ	Degradation index
K_E	Impact energy index	y_{n1}	Input signal received by the hidden layer
W_{ET}	Elastic energy index	y_{o1}	Output value after activating of the hidden layer

1. Introduction

The surrounding rock in underground engineering is subjected to cyclic loading due to mining stress or earthquakes, leading to the degradation of its mechanical properties (Momeni et al., 2015; Zhang et al., 2022a). Therefore, it is imperative to study the degradation mechanisms and variations in rockburst characteristics of rock masses under fatigue loading with different frequencies and stress levels for effective control of surrounding rock in underg`round engineering (Sun et al., 2017; Vaneghi et al., 2018).

A substantial amount of research on the fatigue mechanical properties of rocks has been conducted both domestically and internationally (Xu et al., 2021; Miao et al., 2021). Studies include fatigue loading tests on gypsum rock considering various fatigue elements (Zhu et al., 2021); cyclic loading tests on sandstone, limestone, and quartzite considering

* Corresponding author.
E-mail address: zhangdm@cqu.edu.cn (D. Zhang).

https://doi.org/10.1016/j.rockmb.2024.100171
Received 30 June 2024; Received in revised form 5 August 2024; Accepted 30 November 2024
Available online 30 December 2024

the degradation trend of elastic modulus (Arora et al., 2019); and fatigue life tests of rocks considering the number of induced microcracks (Nejati and Ghazvinian, 2014). In fatigue loading tests, factors such as fatigue stress amplitude, loading frequency, and loading rate significantly influence the fatigue mechanical properties of rocks (Erarslan and Williams, 2012; Song et al., 2022). Regarding fatigue stress amplitude, many researchers have investigated the impact of fatigue stress on rock mechanical properties by varying parameters such as cyclic stress upper limit and stress amplitude (Li et al., 2020a, 2020b). They have also explored stress-strain hysteresis characteristics and hardening effects of rocks under cyclic compression through ultrasonic testing and analysis of fatigue failure mechanisms (Sang et al., 2020). Concerning loading frequency, several studies have analyzed the effect of different fatigue loading frequencies on rock fatigue properties by examining crack evolution, concluding that crack size is negatively correlated with loading frequency (Wang et al., 2021). Other research has used dynamic tests under frequent disturbances at various static axial pressures to analyze the dynamic deformation characteristics, dynamic peak stress-strain, energy changes, and failure modes of serpentinite under high static load frequency (Tang et al., 2016). Zhao et al. (2014) built upon previous work to explore the impact of loading frequency on fatigue life and deformation characteristics of limestone in low-cycle fatigue tests. In terms of loading rate, He et al. (2019) studied damage evolution in salt rock under fatigue loading with different stress amplitudes, loading frequencies, and loading rates. The results indicated that higher stress amplitudes, higher loading frequencies, and faster loading rates all lead to shorter fatigue lives. Additionally, the continuity of cyclic loading during fatigue tests also significantly affects sample fatigue life. Fan et al. (2019) conducted discontinuous cyclic loading tests on salt rock, revealing that fatigue life significantly decreases in discontinuous cyclic compression tests.

Moreover, numerous researchers have developed fatigue mechanical models for rocks based on laboratory data. For instance, a fatigue mechanical model for jointed rock under cyclic conditions has been established to reveal the effects of various cyclic loading parameters on the mechanical properties of jointed rock models (Liu et al., 2018). An empirical fatigue model for salt rock under uniaxial compression conditions has also been developed, which describes the process of irreversible deformation in salt rock using a unified function (Zhang et al., 2022b). Other studies have predicted fatigue life and fatigue strain of rock samples using mathematical models. For example, Haghgouei et al. (2018, 2011) investigated the applicability of bilinear and linear damage rules in rock samples through laboratory fatigue tests and developed a model to predict the fatigue life of green agate samples under fully reversed loading. Xu et al. (2018) derived constitutive equations describing the strain evolution over time during the initial uniform loading phase and the sinusoidal cyclic loading phase based on the real cyclic loading fatigue process of rock samples, using the Poynting-Thomson model, and described the fatigue strain development of salt rock under cyclic loading.

Previous studies have extensively investigated the fatigue characteristics of rocks; however, most have concentrated on high-stress fatigue loading, where the maximum cycling stress exceeds 0.6 times the uniaxial strength (Khaledi et al., 2016; Liu and Dai, 2021; Zhao et al., 2021). In contrast, low-stress fatigue loads, such as those induced by mining and earthquakes, are prevalent in engineering rock masses. Existing research on fatigue damage primarily focuses on analyzing the stress, strain, and energy characteristics of samples during the fatigue process, with limited investigation into the variation in rock mechanical properties before and after fatigue loading. Coal measure strata exhibit numerous weak surfaces and a high degree of dispersion, whereas artificial cast gypsum stone, after prolonged stirring and vibration, possesses a uniform texture with minimal dispersion. Investigating the impact of low-stress fatigue loading on the mechanical properties of samples can mitigate errors caused by rock heterogeneity and yield more consistent results (Wei et al., 2020; Wang et al., 2022a, 2023; Pan et al., 2022). This paper examines the effects of fatigue loading at various frequencies and stress levels on the mechanical properties of samples and the characteristics of rockbursts, using gypsum-like rock as a case study. A mathematical model based on the complex plane was employed to summarize the variation in sample mechanical properties before and after fatigue loading. The research results provide a theoretical reference for managing surrounding rock control in underground engineering subjected to mining stress or other fatigue stresses.

2. Materials and methods

2.1. Sample preparation

Grade α high-strength gypsum powder, manufactured by Sichuan Hongtai Biochemical Co., Ltd., China, was chosen as the material of interest. It primarily consists of $CaSO_4{\cdot}0.5H_2O$. A block was prepared by mixing water and paste in a ratio of 3:10, resulting in a standard sample measuring Φ 50 × 100 mm. The specific preparation process of sample is as follows (Wang, 2021; Wang et al., 2022a, 2022b, 2023):

1) Mold installation: adopt a plastic mold with a side length of 200 mm, apply lubricant to the inside of the mold to facilitate mold removal, and apply Vaseline at the joint to prevent slurry loss; the pouring mold is shown in Fig. 1(a).
2) Weighing and mixing: pour a certain amount of distilled water into a 40-L plastic bucket, pour the weighed gypsum powder evenly into the water, stir the distilled water quickly at the same time, and fully mix it for 60–90 s, shaking the bucket while stirring to reduce bubbles.
3) Production: place the mold on the vibration table, pour the stirred gypsum slurry into the mold, and then stop the shaking table after 2 min.
4) Demolding: when the slurry is completely solidified, cover the surface of the model with fresh-keeping film, and let it react fully. The mold can be demolded after 2 h. The cube sample after demolding is shown in Fig. 1(b).
5) Preparation of standard sample: after the demolded sample is placed for 24 h, it is processed into a standard cylindrical sample of ϕ 50 × 100 mm in the laboratory.

After samples was prepared, XRD-semi-quantitative analysis and conventional triaxial compression test were carried out. The tests results indicate that the sample, under natural conditions, consists of

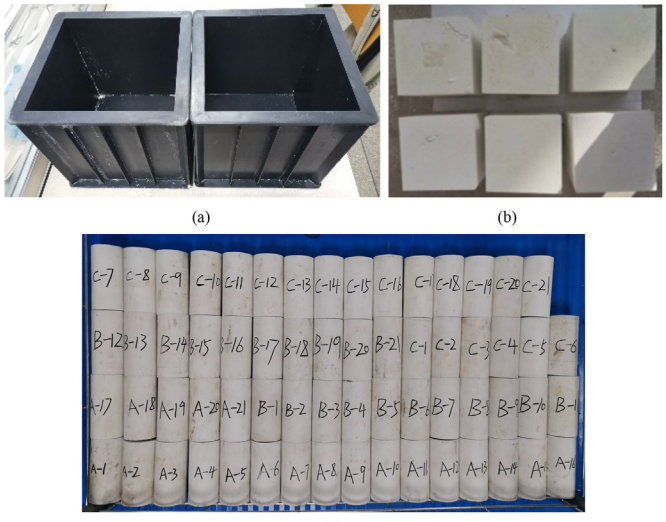

Fig. 1. Remodeled samples of high-strength gypsum powder. (a) Casting mold. (b) Cube samples. (c) Standard samples (Wang et al., 2022a, 2022b).

$CaSO_4{\cdot}2H_2O$ and $CaSO_4{\cdot}0.5H_2O$. It exhibits a density (ρ) of 1.8 g/cm^3, a *P*-wave velocity of 2967 m/s, a water content (f_w) of 0.254, a cohesion (c) of 13.18 MPa, an internal friction angle (φ) of 27°, a uniaxial compressive strength (σ_c) of 44.53 MPa, and a tensile strength (σ_t) of 3.85 MPa (Wei et al., 2020; Wang et al., 2023).

2.2. Test devices

1) RMT-150B electro-hydraulic servo rock test system, as shown in Fig. 2(a). The maximum axial load of the system is 1000 kN, the maximum displacement is 5 mm, and the deformation accuracy is 1.0 $\times$ 10^{-3} mm.
2) QKX-YD-1000 electro-hydraulic servo rock dynamic fatigue test system, as shown in Fig. 2(c). The maximum axial load of the system is 800 kN, the maximum displacement is 50 mm, and the fatigue frequency range is 0.5–50 Hz.

2.3. Test method

2.3.1. Grouping

The samples were divided into 20 groups, 6 samples in each group, for the fatigue loading test. The fatigue test had a fixed loading amplitude (A) of 0.1 σ_c (where σ_c represents the uniaxial compressive strength before fatigue loading). The central value of fatigue loading (C) ranged from 0.2 σ_c to 0.8 σ_c, with loading frequencies (f) of 1, 2, 4, 10, and 20 Hz, and a loading time (t) of 500 s. Refer to Table 1 for details.

2.3.2. Fatigue loading tests

The fatigue loading test was carried out on the QKX-YD-1000 electro-hydraulic servo rock dynamic fatigue test system. Fatigue loading of samples for each group was carried out according to the scheme in Table 1. The force control mode was employed with a loading rate of 0.5 kN/s. Initially, the sample was loaded to the central value of fatigue loading (C). Subsequently, fatigue loading is applied using a sinusoidal waveform, as shown in Fig. 3.

2.3.3. Mechanical tests

Following fatigue loading, the samples were divided into two groups (3 samples in each group), underwent uniaxial compression tests and loading-unloading tests using the RMT-150B electro-hydraulic servo rock test system. The uniaxial compression test was conducted using a displacement control mode, with a loading rate of 0.005 mm/s. The loading-unloading test was performed using force control mode with a loading rate of 0.5 kN/s. The axial force was loaded to 0.75 σ_c and then unloaded. Subsequently, the uniaxial compression strength, peak strain, impact energy index, elastic energy index, and other parameters of the samples after fatigue loading were determined. The calculation method for the impact energy index can be found in Fig. 4.

In this study, the uniaxial compression tests utilize constant displacement loading, resulting in a varying force on the top of the sample. For example, using Fig. 4 as a reference, the energy stored in the sample during loading can be calculated by first converting the σ-ε curve into the F-x curve, and then applying the calculus method as follows:

$$W_1 = \int_0^{x_c} F(x)dx \tag{1}$$

where W_1 is the energy accumulated during the sample's loading process and x_c is the strain at the peak stress.

Due to the unknown function expression of $F(x)$, Eq. (1) cannot be solved directly. Here, we introduce an infinitesimally small quantity ($\triangle x$, the difference in displacement between every two adjacent sampling points), dividing the $F(x)$ curve into an infinite number of small rectangles, and calculating the sum of the areas of each rectangle. This can be expressed as:

$$W_1 = \int_0^{x_c} F(x)dx = \sum_{n=0}^{x_c} \triangle x \cdot \frac{[F(n) + F(n+\triangle x)]}{2}, \{ m \in N \ (Number\ set) \tag{2}$$

where x_c is the strain corresponding to the peak strength of the sample, $n = m \cdot \triangle x$, m is a continuous natural number.

Similarly, the expression for W_2 is easy to obtain. Then, the formula for calculating the impact energy index K_E is as follows:

$$K_E = \frac{W_1}{W_2} = \frac{\sum_{n=0}^{x_c} [F(n) + F(n+\triangle x)]}{\sum_{n=x_c}^{x_e} [F(n) + F(n+\triangle x)]} \tag{3}$$

where W_1 is the energy stored during loading and W_2 is the energy released during unloading.

When calculating the elastic energy index (W_{ET}), the energy accumulated during loading and the energy released during unloading can be calculated according to the above method, and then solved, not tired in words here.

2.3.4. Technology roadmap

The above test methods are summarized and the technical roadmap is drawn as shown in Fig. 5. All mechanical tests in this study were carried out at room temperature.

Table 1
The test parameters of fatigue loading tests.

Group	C ($n\cdot\sigma_c$)	A ($n\cdot\sigma_c$)	f (Hz)	t (s)
20 (4 × 5)	0.2, 0.4, 0.6, 0.8	0.1	1, 2, 4, 10, 20	500

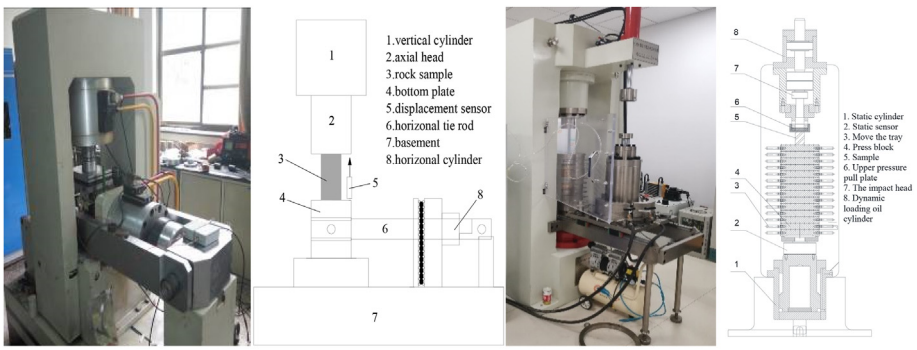

(a) (b) (c) (d)

Fig. 2. Mechanical testing devices. (a) RMT-150B test system. (b) RMT-150B schematic diagram. (c) QKX-YD-1000 test system. (d) QKX-YD-1000 schematic diagram.

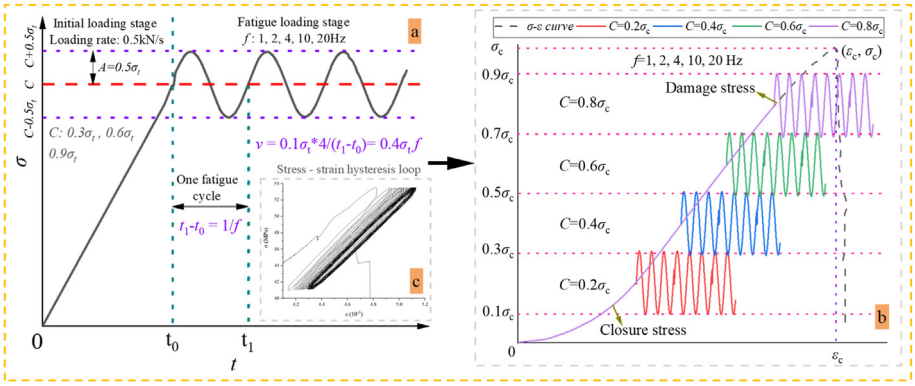

Fig. 3. Fatigue loading test stress path with different stress range and frequency: $C = 0.2\ \sigma_c$, $0.4\ \sigma_c$, $0.6\ \sigma_c$, $0.8\ \sigma_c$; $f = 1$, 2, 4, 10, 20 Hz. (a) Stress path. (b) Stress range. (c) Stress-strain hysteresis loop.

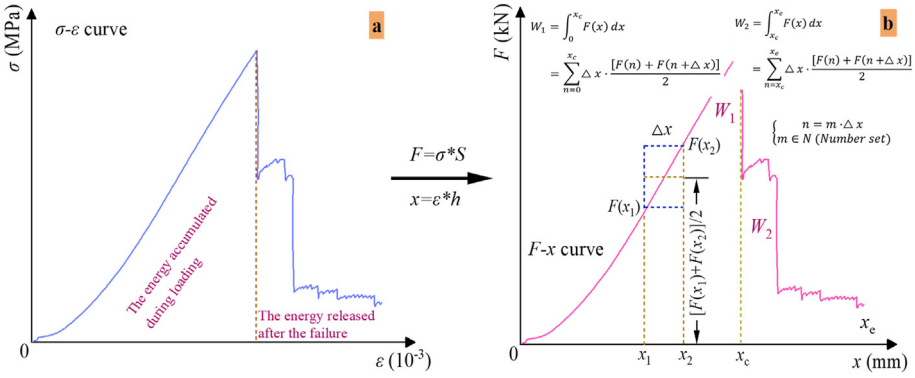

Fig. 4. The calculation method of impact energy index. (a) σ-ε curve. (b) F-x curve.

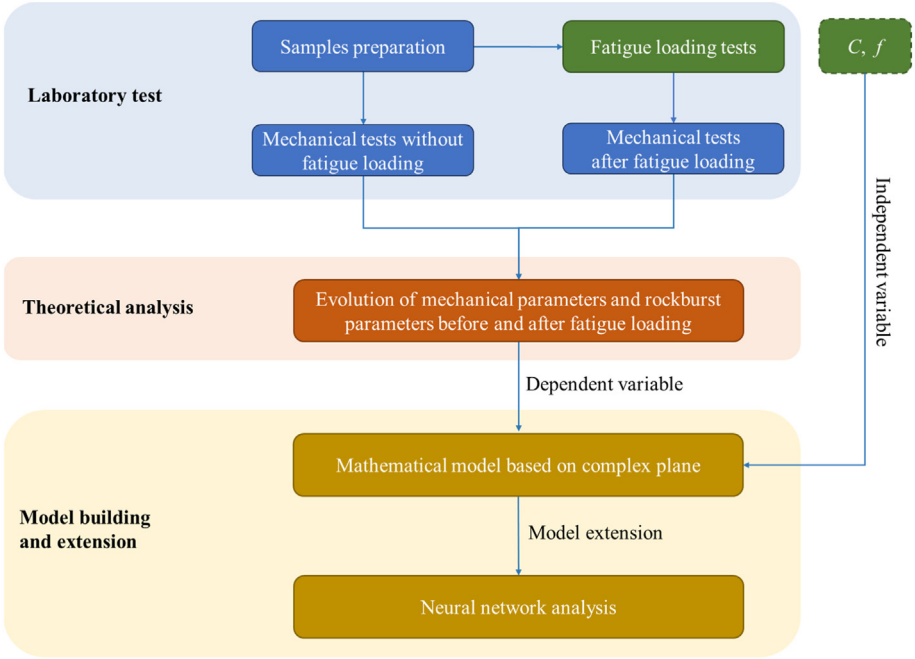

Fig. 5. Technical roadmap for the study of rock mechanical parameter evolution before and after fatigue loading.

3. Test results and analysis

Previous studies (Wang et al., 2022a) have analyzed the fatigue characteristics of the samples during fatigue loading. This study primarily focuses on presenting the evolution of mechanical properties and rockburst proneness of samples before and after fatigue loading tests. Among them, the main parameters to evaluate the rockburst tendency of the sample are impact energy index and elastic energy index, and the

greater the two, the greater the rockburst tendency of the sample. Table 2 displays the mechanical parameters of the typical samples before and after fatigue loading, including the uniaxial compressive strength after fatigue loading (σ_{cf}), peak strain (ε_c), impact energy index (K_E), and elastic energy index (W_{ET}). The literature (Wang et al., 2022b) presents the stress-strain curves of the typical sample of each group before and after fatigue loading. The typical sample is one with an intermediate peak strength. It is important to note that when $C = 0.8\ \sigma_c$ and $f = 1$ Hz, all samples were destroyed during fatigue loading, resulting in a lack of post-fatigue test data under these conditions (Wang et al., 2022a). The changes in the mechanical characteristics of the sample after fatigue stress loading with different stress range and frequencies are as follows:

1) Fatigue loading at 0.1 σ_c-0.3 σ_c has a limited impact on the mechanical properties of the samples. At frequencies of 1 and 2 Hz, σ_{cf} decreases by 7.77% and 24.7%, respectively, while K_E decreases by 45.3% and 22.1%, respectively, compared to the samples without fatigue loading. Conversely, at frequencies of 4 Hz, 10 Hz, and 20 Hz, σ_{cf} increases by 0.7%, 11.1%, and 14.0%, respectively, while K_E increases by 380%, 433%, and 44.2%, respectively. The above conclusion indicates that under $C = 0.2\ \sigma_c$ and at low frequencies ($f =$ 1 or 2 Hz), fatigue loading weakens the performance of the sample, specifically the uniaxial compressive strength and impact energy index, to varying degrees. Conversely, at higher frequencies ($f = 4$, 10, 20 Hz), the effect of fatigue loading is intensified, resulting in an increase in uniaxial strength and impact energy index after cyclic loading.
2) Following fatigue loading at 0.3 σ_c–0.5 σ_c, σ_{cf} exhibits minimal change compared to the peak strength before fatigue. On average, K_E decreased by 69.1% compared to group I. Additionally, K_E demonstrated a decreasing trend compared to the samples without fatigue loading, particularly at frequencies of 1 and 2 Hz, with a decrease of approximately 49%. The above analysis indicates that the fatigue load at $C = 0.4\ \sigma_c$ has a significant influence on the sample, resulting in a notable decrease in the impact energy index, thereby reducing the rockburst tendency.
3) Following fatigue loading at 0.5 σ_c–0.7 σ_c, σ_{cf} increased in all samples except for the one with $f = 2$ Hz. Notably, at frequencies of 4, 10, and 20 Hz, K_E experiences significant increases, surpassing those observed in other group samples. These findings demonstrate that when subjected to a fatigue load of C = 0.6 σ_c, high frequency fatigue loading ($f = 4$, 10, or 20 Hz) induces substantial changes in the sample's properties, resulting in a significant increase in the impact energy index and a surge in the rockburst tendency.
4) Following fatigue loading at 0.7 σ_c–0.9 σ_c, σ_c' decreases in each sample. At frequencies of 2, 4, 10, and 20 Hz, K_E values experience a significant increase to 90.24, 101.6, 98.22, and 89.95, respectively. These results indicate that fatigue loading at $C = 0.8\ \sigma_c$ has a notable effect on the sample, resulting in a reduction in compressive strength and an increase in rockburst tendency.

Table 2
Mechanical parameters of gypsum-like samples before and after fatigue loading (Wang, 2021).

Group	C	f (Hz)	σ_{cf} (MPa)	ε_c (10^{-3})	K_E	W_{ET}
	Before fatigue		45.7	4.31	1.72	2.78
I	$0.2\sigma_c$	1	42.2	3.85	0.94	3.64
		2	34.4	3.3	1.34	3.97
		4	46	4.19	8.26	3.56
		10	50.8	4.43	9.17	3.25
		20	52.1	4.74	2.48	3.62
II	$0.4\sigma_c$	1	47.4	4.51	0.87	2.86
		2	41.5	4.39	0.88	3.44
		4	48.4	4.09	1.03	2.44
		10	47.2	4.37	2.59	2.86
		20	44.2	3.9	1.49	1.17
III	$0.6\sigma_c$	1	48.7	4.28	1.63	2.64
		2	43.1	4.99	2.45	2.63
		4	49.7	4.97	79.93	2.48
		10	45.6	4.74	80.69	2.53
		20	50.3	4.84	74.65	1.67
IV	$0.8\sigma_c$	1	–	–	–	–
		2	38.2	3.93	90.24	1.93
		4	39.6	4.18	101.6	2.02
		10	39.1	4.23	98.22	1.92
		20	39.5	4.38	89.95	1.89

As observed in Table 2, W_{ET} in the I and III sample sets exhibits minimal variation at low frequencies, but experiences a significant reduction after $f = 10$ Hz. In the II sample set, low frequencies result in a slight increase in W_{ET}, whereas with increasing frequency, W_{ET} decreases. Particularly at $f = 20$ Hz, the peak strain reached nearly 5‰, and W_{ET} decreased to 1.2. W_{ET} exhibited a downward trend in the IV groups. This can be explained by the gradual decrease in the elastic energy accumulated in the rock sample with increasing fatigue frequency. As the sample is loaded to 0.7 σ_c, its deformation gradually increases, and the transient elastic strain continuously decreases after unloading. Consequently, the ratio of elastic energy to plastic energy consumption in the sample decreases with increasing loading frequency, which is reflected in the loading and unloading curve as a right inclination and a decrease in the elastic energy index, and the rockburst tendency of the sample decreases.

The above results indicate that during fatigue loading, the effects of cyclic stress and loading frequency on the mechanical properties and rockburst parameters of the samples are interrelated. The effect of fatigue cyclic stress on the mechanical parameters and rockburst parameters of the samples after fatigue loading is relatively straightforward: the greater the cyclic stress, the higher the impact energy index, the lower the elastic energy index, and the greater the rockburst tendency of the samples after fatigue loading. However, the impact of frequency on the mechanical properties of samples after fatigue loading is more complex. At low cyclic stress (0.1 σ_c–0.7 σ_c), the frequency significantly affects the fatigue damage characteristics of the samples, with substantial changes in the rockburst parameters as the frequency varies. In contrast, at high cyclic stress (0.7 σ_c–0.9 σ_c), the impact of frequency on the fatigue damage characteristics of the samples is considerably reduced compared to cyclic stress, and the fatigue damage of the samples slightly decreases with increasing frequency.

This result is similar to some previous studies. For instance, Zhao et al. (2014) discovered in fatigue tests on limestone that the fatigue life of samples increased with increasing loading frequency, Ishizuka and Abe (1990) found analogous conclusions in their research on the fatigue life of granite. This suggests that, under certain conditions, increasing frequency in fatigue loading tests reduces the fatigue damage of rocks. However, some scholars believe that fatigue frequency increases the fatigue damage of samples (Li et al., 2001; Jiang, 2003). The innovation of this paper lies in identifying the conditions under which frequency affects the fatigue damage of samples. Specifically, under high cyclic stress (0.7 σ_c–0.9 σ_c), increasing frequency reduces the fatigue damage of samples; under low cyclic stress (0.1 σ_c–0.7 σ_c), the influence of frequency on the fatigue damage of samples exhibits complex and nonlinear characteristics.

4. Establishment of degradation index model

To quantitatively analyze the degradation mechanism of samples subjected to fatigue load, a sample degradation index (λ) was introduced. This index considers four parameters: uniaxial compressive strength (MPa), peak strain (10^{-3}), impact energy index, and elastic energy index. The expressions are as follows:

$$\lambda \propto f\left(\triangle \sigma_{cf},\ \triangle \varepsilon_c,\ \triangle K_{\mathrm{E}},\ \triangle W_{\mathrm{ET}}\right) \tag{4}$$

The derivation process of sample degradation index (λ) is shown in Fig. 6.

Uniaxial compressive strength and peak strain represent direct rock mechanical parameters, while impact energy index and elastic energy index serve as indicators of rockburst tendency. These two kinds of parameters are not entirely independent. To enhance the scientific rigor of the formula, the imaginary part j is introduced into Eq. (4), denoted as:

$$\lambda \propto \{ f\left(\triangle \sigma_{cf},\ \triangle \varepsilon_c\right) + j \cdot g(\triangle K_{\mathrm{E}},\ \triangle W_{\mathrm{ET}}) \} \tag{5}$$

It can be seen from Table 2 that mechanical and rockburst parameters of the sample before fatigue test were:

$$\{\sigma_{c0},\ \varepsilon_{c0},\ K_{\mathrm{E0}},\ W_{\mathrm{ET0}}\} = \{45.7, 4.31, 1.72, 2.78\} \tag{6}$$

For simple calculation, the relationship between the growth rate of each parameter and deterioration index was explored. Eq. (5) can be written as:

$$\lambda \propto \{ f\left(\sigma_{cf}^{'}, \varepsilon_c^{'}\right) + j \cdot g\left(K_{\mathrm{E}}^{'}, W_{\mathrm{ET}}^{'}\right) \} \tag{7}$$

where, $\sigma_{cf}^{'} = \frac{\sigma_c - \sigma_{c0}}{\sigma_{c0}}$, $\varepsilon_c^{'} = \frac{\varepsilon_c - \varepsilon_{c0}}{\varepsilon_{c0}}$, $K_E^{'} = \frac{K_{\mathrm{E}} - K_{\mathrm{E0}}}{K_{\mathrm{E0}}}$, $W_{\mathrm{ET}}^{'} = \frac{W_{\mathrm{ET}} - W_{\mathrm{ET0}}}{W_{\mathrm{ET0}}}$.

The growth rate of each parameter in Table 2 after fatigue loading was calculated step by step, using the parameters before fatigue in Eq. (3) as reference. The results are presented in Table 3, with negative values indicating a decrease.

Currently, there are several widely used nonlinear surface fitting functions, including Chebyshev^{2D}, Fourier^{2D}, Gaussian^{2D}, and others. In this study, Parabola^{2D} was chosen to fit the mechanical parameters after observing the three-dimensional scatter diagram of each data group in Table 3. The Parabola^{2D} function is expressed as follows:

$$z = a + bC + lf + mC^2 + nf^2 \tag{8}$$

where a, b, l, m, and n are fitting parameters.

Table 3
Growth rate of mechanical and rockburst parameters of samples before and after fatigue loading.

C	f/Hz	$\sigma_{cf}^{'}$	$\varepsilon_c^{'}$	$K_{\mathrm{E}}^{'}$	$W_{\mathrm{ET}}^{'}$	$E_{\mathrm{T}}^{'}$
Before fatigue		0	0	0	0	0
$0.2\sigma_c$	1	−0.077	−0.107	−0.453	0.309	0.098
	2	−0.247	−0.234	−0.221	0.428	0.054
	4	0.007	−0.028	3.802	0.281	0.000
	10	0.112	0.028	4.331	0.169	0.036
	20	0.140	0.100	0.442	0.302	0.179
$0.4\sigma_c$	1	0.037	0.046	−0.494	0.029	0.214
	2	−0.092	0.019	−0.488	0.237	0.188
	4	0.059	−0.051	−0.401	−0.122	0.188
	10	0.033	0.014	0.506	0.029	0.268
	20	−0.033	−0.095	−0.134	−0.579	0.375
$0.6\sigma_c$	1	0.066	−0.007	−0.052	−0.050	0.205
	2	−0.057	0.158	0.424	−0.054	0.134
	4	0.088	0.153	45.471	−0.108	0.071
	10	−0.002	0.100	45.913	−0.090	0.036
	20	0.101	0.123	42.401	−0.399	0.170
$0.8\sigma_c$	1	–	–	–	–	–
	2	−0.164	−0.088	51.465	−0.306	0.080
	4	−0.133	−0.030	58.070	−0.273	0.116
	10	−0.144	−0.019	56.105	−0.309	0.063
	20	−0.136	0.016	51.297	−0.320	0.134

Parabola 2D function was used to fit the four growth rate indicators $\{\sigma_{cf}^{'}(C,f), \varepsilon_c^{'}(C,f), K_{\mathrm{E}}^{'}(C,f), W_{\mathrm{ET}}^{'}(C,f)\}$, as shown in Fig. 7.

The fitting formula of the four spatial functions is as follows:

$$\begin{cases} \sigma_{cf}^{'} = a_1 + b_1 C + l_1 f + m_1 C^2 + n_1 f^2 \\ \varepsilon_c^{'} = a_2 + b_2 C + l_2 f + m_2 C^2 + n_2 f^2 \\ K_{\mathrm{E}}^{'} = a_3 + b_3 C + l_3 f + m_3 C^2 + n_3 f^2 \\ W_{\mathrm{ET}}^{'} = a_4 + b_4 C + l_4 f + m_4 C^2 + n_4 f^2 \end{cases} \tag{9}$$

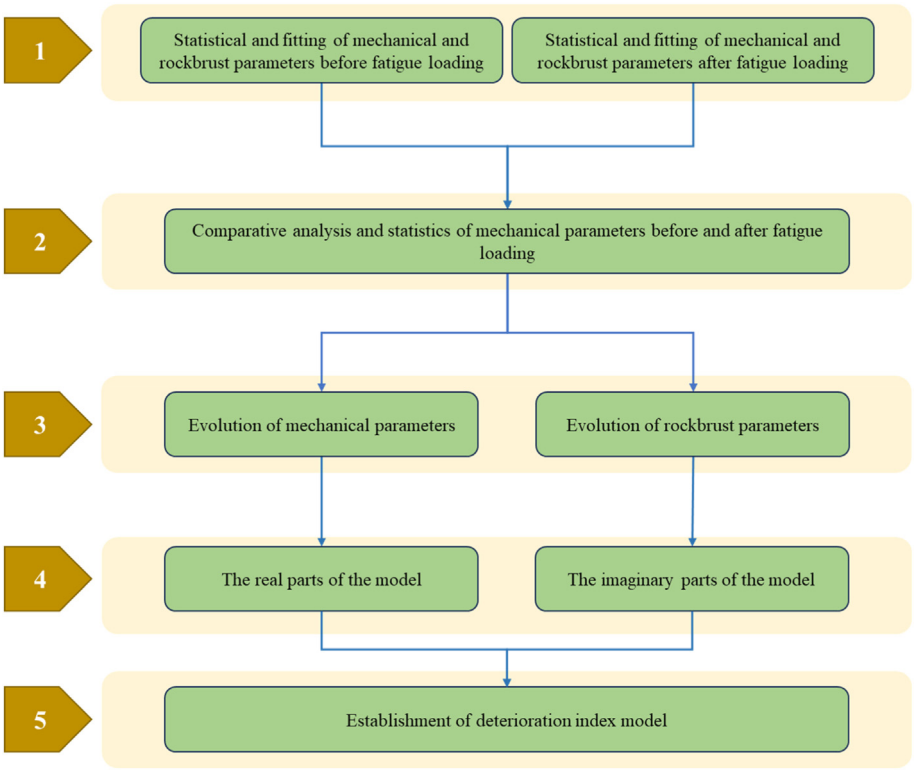

Fig. 6. Derivation process of samples degradation index (λ).

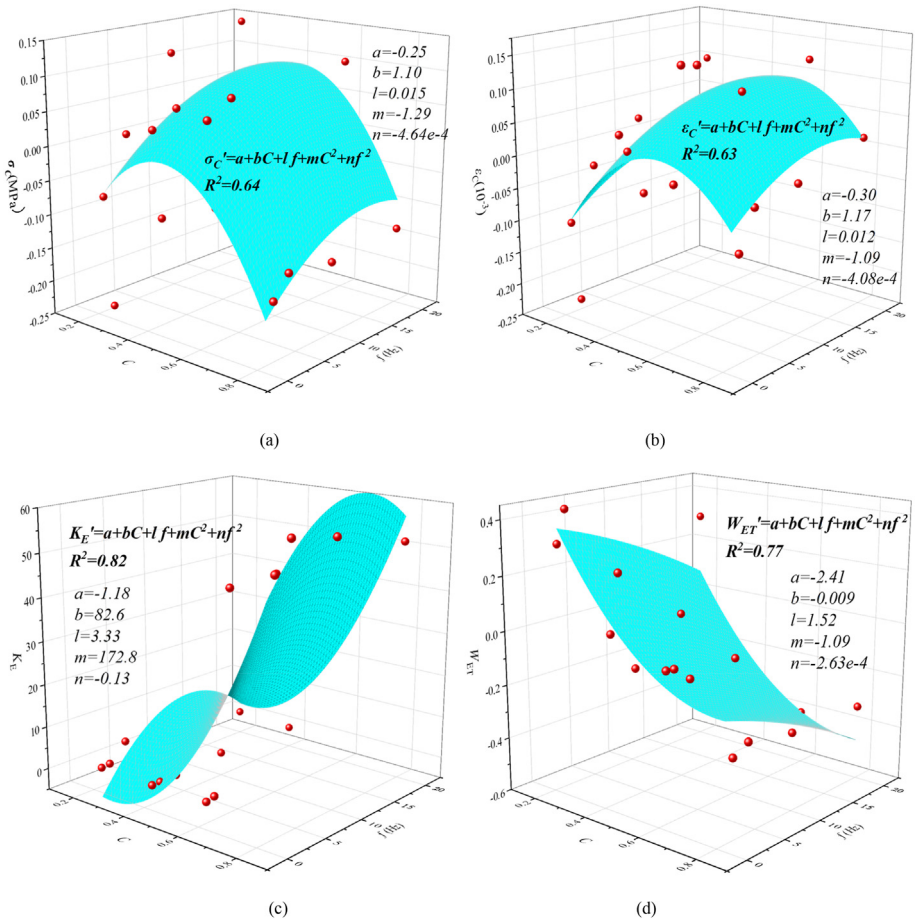

Fig. 7. The fitting of mechanical parameters and rockburst parameters of samples before and after fatigue loading. (a) $\sigma_{cf}^{'}(C,f)$. (b) $\varepsilon_{c}^{'}(C,f)$. (c) $K_{\mathrm{E}}^{'}(C,f)$. (d) $W_{\mathrm{ET}}^{'}(C,f)$.

In Eq. (9), the values of each parameter are as follows:

$$\begin{cases} a^T = -(0.25 \quad 0.30\ 1.18 \quad 2.41)^T \\ b^T = (1.10 \quad 1.17\ 82.6 \quad -0.009)^T \\ l^T = (0.015 \quad 0.012\ 3.33 \quad 1.52)^T \\ m^T = (-1.29 \quad -1.09\ 172.8 \quad -1.09)^T \end{cases}$$

$$n^T = -(4.64e-4 \quad 4.08e-4\ 0.13 \quad 2.63e-4)^T$$

A higher uniaxial strength indicates a stronger rock compressive ability. Similarly, a larger peak strain corresponds to better rock ductility. Consequently, the deterioration index exhibits a negative correlation with rock mass strength and peak strain, as follows:

$$\begin{cases} \lambda \propto 1/\sigma_{cf}^{'} \\ \lambda \propto 1/\varepsilon_{c}^{'} \end{cases} \tag{10}$$

Thus, the real part function is constructed:

$$f\left(\sigma_{cf}^{'},\varepsilon_{c}^{'}\right) \propto 1 \Big/ \left(\sigma_{cf}^{'}+\varepsilon_{c}^{'}\right) \tag{11}$$

Considering that $\sigma_{cf}^{'}$ and $\varepsilon_{c}^{'}$ are functions that pass through zero, it is important to note that dividing a large number by a decimal can lead to increased error, as per the principle of numerical analysis. Consequently, to adjust the function, new parameters p and q are introduced, denoted as:

$$f\left(\sigma_{cf}^{'},\varepsilon_{c}^{'}\right) \propto \left[1 \Big/ \left(\sigma_{cf}^{'}+\varepsilon_{c}^{'}+p\right)-q\right] \tag{12}$$

Parameter p shifts the divisor part $(\sigma_{c}^{'}+\varepsilon_{c}^{'})$ of the function away from the origin, while parameter q repositions the image of the function closer to the origin.

$$f\left(\sigma_{cf}^{'},\varepsilon_{c}^{'}\right)=\frac{1}{(a_1+a_2)+(b_1+b_2)C+(l_1+l_2)f+(m_1+m_2)C^2+(n_1+n_2)f^2+p}-q \tag{13}$$

By combining the parameters, it can be obtained:

$$f\left(\sigma_{cf}^{'},\varepsilon_{c}^{'}\right)=\frac{1}{A_1+B_1C+L_1f+M_1C^2+N_1f^2+p}-q \tag{14}$$

where, $A_1 = a_1 + a_2$, $B_1 = b_1 + b_2$, …, $N_1 = n_1 + n_2$. Namely: $A_1 = -0.55, B_1 = 2.28, L_1 = 0.027, M_1 = -2.38, N_1 = -8.72\mathrm{e}^{-4}$

Substitute in the values of each variable, and let $p = 2$, $q = -0.5$, then:

$$f\left(\sigma_{cf}^{'},\varepsilon_{c}^{'}\right)=\frac{1}{1.45+2.28C+0.027f-2.38C^2-0.000872f^2}-\frac{1}{2} \tag{15}$$

The impact energy index and elastic energy index serve as parameters that indicate rock bursting tendency. A higher value of these indices indicates a stronger rock bursting tendency and greater instability in rock properties. Therefore, $\lambda \propto K_{\mathrm{E}}^{'}$, $\lambda \propto W_{\mathrm{ET}}^{'}$.

Thus, the imaginary part function is constructed:

$$jg\left(K_{\mathrm{E}}^{'},W_{\mathrm{ET}}^{'}\right) \propto jy \cdot \left(K_{\mathrm{E}}^{'}+W_{\mathrm{ET}}^{'}\right) \tag{16}$$

To maintain consistency between the magnitude of the imaginary part and the real part, the parameter $r = 5\times 10^3$ is introduced as the denominator. Subsequently,

$$jg\left(K_{\mathrm{E}}^{'}, W_{\mathrm{ET}}^{'}\right) \propto jy \cdot \frac{K_{\mathrm{E}}^{'}+W_{\mathrm{ET}}^{'}}{r} \tag{17}$$

$$jg\left(K_{\mathrm{E}}^{'}, W_{\mathrm{ET}}^{'}\right) = j\frac{\left[(a_3+a_4)+(b_3+b_4)C+(l_3+l_4)f+(m_3+m_4)C^2+(n_3+n_4)f^2\right]}{r} \tag{18}$$

By combining the parameters, it can be obtained:

$$jg\left(K_{\mathrm{E}}^{'}, W_{\mathrm{ET}}^{'}\right) = \frac{j\left(A_2 + B_2C + L_2f + M_2C^2 + N_2f^2\right)}{r} \tag{19}$$

where, $A_2 = a_3 + a_4$, $B_2 = b_3 + b_4$, …, $N_2 = n_3 + n_4$; namely: $A_2 = 3.59$, $B_2 = 82.6, L_2 = 4.85, M_2 = 171.71, N_1 = -0.13$.

Substitute in the values of each variable, it can be obtained:

$$jg\left(K_{\mathrm{E}}^{'}, W_{\mathrm{ET}}^{'}\right) = \frac{j\left(3.59 + 82.6C + 4.85f + 171.71C^2 - 0.13f^2\right)}{5000} \tag{20}$$

Thus, the expression of deterioration parameter can be obtained as:

$$\lambda = -\frac{1}{2} + \frac{1}{1.45 + 2.28C + 0.027f - 2.38C^2 - 0.000872f^2} + j\frac{3.59 + 82.6C + 4.85f + 171.71C^2 - 0.13f^2}{5000} \tag{21}$$

Equation (21) represents the expression of the deterioration index. The real part of the function represents the deterioration degree of mechanical properties of the rock mass, while the imaginary part represents the deterioration degree of rockburst parameters. The modulus $|\lambda|$ of the function signifies the overall variation in both mechanical properties and rockburst properties of the rock mass following fatigue loading.

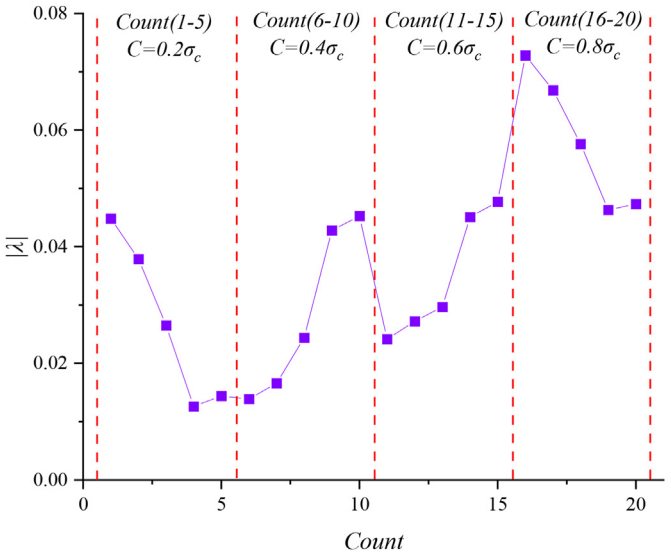

Fig. 8. Absolute changes of rock mechanics and rockburst parameters before and after fatigue loading.

magnitude of $|\lambda|$ merely indicates the sum of absolute changes in the two sample properties and does not directly reflect the degree of deterioration in the sample.

Figs. 8 and 9 demonstrate the repetitive fluctuations of $|\lambda|$ within the range of 0–0.002 throughout count (1)–count (15). During count (4)–count (7), there is a gradual increase in $g\left(K_{\mathrm{E}}^{'}, W_{\mathrm{ET}}^{'}\right)$, accompanied by a decrease in F towards 0, resulting in a decline of $|\lambda|$ to its lowest point. This suggests that the fatigue loading within this range has minimal impact on the overall mechanical properties of the sample. Notably, during count (9)–count (10), there is a steady rise in $g\left(K_{\mathrm{E}}^{'}, W_{\mathrm{ET}}^{'}\right)$

$$|\lambda| = \sqrt{\left(\frac{1}{1.45 + 2.28C + 0.027f - 2.38C^2 - 0.000872f^2} - \frac{1}{2}\right)^2 + \left(\frac{3.59 + 82.6C + 4.85f + 171.71C^2 - 0.13f^2}{5000}\right)^2} \tag{22}$$

accompanied by a negative increase in $f(\sigma_{cf}^{'}, \varepsilon_c^{'})$, indicating a decline in mechanical properties and a decrease in rockburst tendency, albeit with an overall increase in the variation range. During count (15)–count (16), there is a notable surge in $|\lambda|$ due to the rapid growth observed in both $f(\sigma_{cf}^{'}, \varepsilon_c^{'})$ and $g\left(K_{\mathrm{E}}^{'}, W_{\mathrm{ET}}^{'}\right)$. Subsequently, as $f(\sigma_{cf}^{'}, \varepsilon_c^{'})$ decreases, $|\lambda|$ also decreases.

Based on the findings from Figs. 8 and 9, the complex plane function image of the deterioration index is illustrated in Fig. 10. In the figure, count (1)–count (20) is represented along the vertical axis, progressing from bottom to top. Fig. 10 exhibits a close relationship with Figs. 8 and 9. The distance from each point to the origin in Fig. 10 represents the length of the longitudinal axis ($|\lambda|$) in Fig. 8. Furthermore, Fig. 10 represents the projection of Fig. 9 onto the (Real Part, Imaginary Part) plane, providing a compressed visualization of its Count (n) axis. From Fig. 10, we can clearly observe the variation patterns in mechanical properties and rockburst characteristics of samples under different (C, f) conditions before and after fatigue loading. Moreover, the position of the λ curve in the model allows for an understanding of their overall variation characteristics.

To represent the real and imaginary parts of the function in a coordinate system, the independent variables (C, f) are unified, and the count (n) function is introduced. Let us define:

$$Count\ (n) = (C_n, f_n) \tag{23}$$

In Eq. (23), Count (n) is incrementally superimposed based on the central value and frequencies of fatigue loading. Specifically,

$$Count\ (1) = (0.2, 1),\ Count\ (2) = (0.2, 2),\ \ldots,\ Count\ (6) = (0.4, 1),\ \ldots,\ Count\ (20) = (0.8, 20) \tag{24}$$

The values of (C, f) were sequentially substituted into Eqs. (21) and (22) based on the laboratory test scheme. Subsequently, the calculations for $f(\sigma_{cf}^{'}, \varepsilon_c^{'})$, $g\left(K_{\mathrm{E}}^{'}, W_{\mathrm{ET}}^{'}\right)$, and $|\lambda|$ were performed, and the resulting curves were plotted as depicted in Figs. 8 and 9.

Fig. 8 illustrates the absolute variation in rock properties, while Fig. 9 depicts the specific variation characteristics of both mechanical properties and rockburst properties. It is important to note that the real part of the deterioration index, which serves as the characterization parameter for mechanical properties, may not always be positive. Hence, the

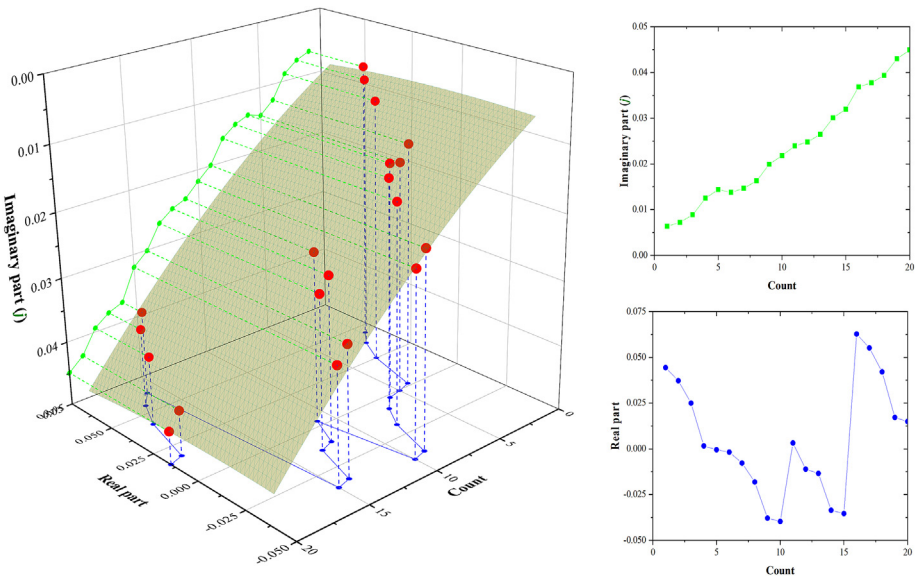

Fig. 9. Deterioration index model of samples before and after fatigue loading. (a) Relationship between real part, imaginary part, and Count (n).

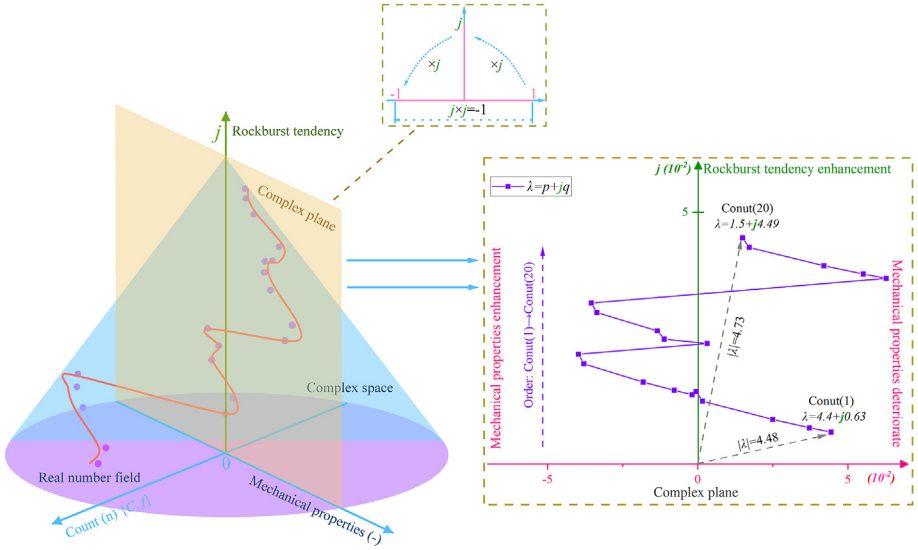

Fig. 10. Degradation index model of samples after fatigue loading: $\lambda = p + jq$. (a) Degradation index curve in complex space. (b) Complex axis diagram. (c) Degradation index curve in complex plane.

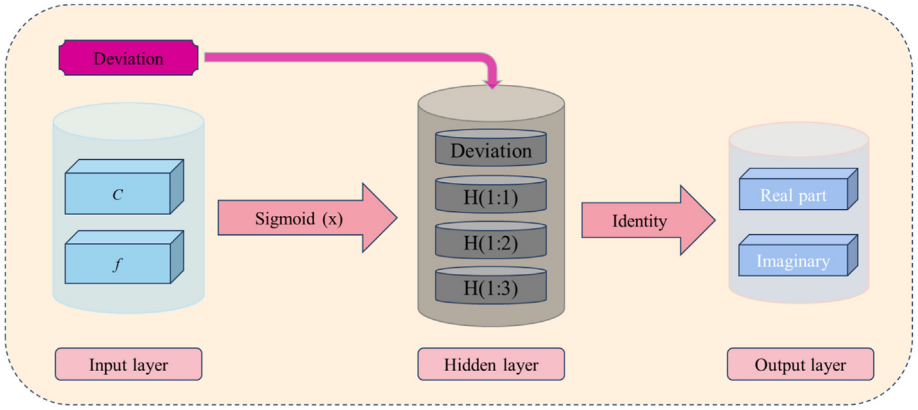

Fig. 11. The neural network model based on multi-layer perceptron.

5. Model expansion and visualization based on neural network analysis

Section 4 analyzes the impact of fatigue loading with varying C and f values on rock mechanical properties within the complex plane range and introduces a mathematical model based on the complex plane. However, direct application and generalization of this model is challenging. To enhance the practicality of the model and validate its results, this section establishes a neural network model based on section 4. This approach facilitates data input and model promotion, as supported by previous studies (Das and Basudhar, 2008; Hu et al., 2022, 2023).

Fig. 11 illustrates the neural network model based on a multi-layer perceptron. In the input layer of Fig. 11, the respective weights assigned to C and f are 0.723 and 0.383. This suggests that the fatigue stress level exerts a stronger influence on rock mechanical properties, aligning with the findings from the previous analysis.

In Fig. 11, the hidden layer activation function of multilayer perceptron is $sigmoid(x)$, namely:

$$sigmoid(x) = \frac{1}{1+e^{-x}} \tag{25}$$

The weight calculation method for each layer is as follows:

Calculate the weighted sum of input factors (C, f) along with the error between the output result of the hidden layer and the actual result:

$$\begin{cases} R = (Y_{ta} - Y_{o1})^2 \\ y_{o1} = \dfrac{1}{(1+e^{-y_{n1}})} \\ y_{n1} = x_1 + x_2 + x_3 \end{cases} \tag{26}$$

where, R is the error; y_{n1} is the input signal received by the hidden layer; y_{o1} is the output value after activating of the hidden layer.

2) Update weight:

Using w_1 as an example, its weight is updated following error back-propagation, necessitating the calculation of the partial derivative of w_1 with respect to the overall error, denoted as $\partial R/\partial w_1$. To facilitate computation, $\partial R/\partial w_1$ can be decomposed.

$$\frac{\partial R}{\partial w_1} = \frac{\partial R}{\partial y_{o1}} \cdot \frac{\partial y_{o1}}{\partial y_{n1}} \cdot \frac{\partial y_{n1}}{\partial w_1} \tag{27}$$

Because:

$$\begin{cases} \dfrac{\partial R}{\partial y_{o1}} = 2(Y_{o1} - Y_{ta}) \\ \dfrac{\partial y_{o1}}{\partial y_{n1}} = \dfrac{e^{-y_{n1}}}{(1+e^{-y_{n1}})^2} = \dfrac{1}{1+e^{-y_{n1}}}\left(1 - \dfrac{1}{1+e^{-y_{n1}}}\right) \\ \dfrac{\partial y_{n1}}{\partial w_1} = \dfrac{\partial (w_1 x_1 + w_2 x_2 + w_3 x_3)}{\partial w_1} = x_1 \end{cases} \tag{28}$$

So:

$$\frac{\partial R}{\partial w_1} = (Y_{o1} - Y_{ta}) \cdot \left[\frac{1}{1+e^{-y_{n1}}}\left(1 - \frac{1}{1+e^{-y_{n1}}}\right)\right] \cdot x_1 \tag{29}$$

Using the calculation results of Eq. (29), update the value of w_1:

$$w_1' = w_1 - \eta \cdot \frac{\partial R}{\partial w_1} \tag{30}$$

The weights of all synapses in the model are derived by iteratively performing the steps (Algorithm 1 is a weight training method taking "Real part" as an example). The model was used to fit the real part and imaginary part of complex plane under different C and f conditions, as shown in Fig. 12.

Algorithm 1. Model training

Input: C, f, Training number N
Output: Weight w_1, w_2
1: $w_1 \leftarrow 0.1$, $w_2 \leftarrow 0.1$
2: **for** $i \leftarrow 0$ to $N-1$ **do**
3: $S \leftarrow w_1\, C[i] + w_2\, f[i]$
4: $Y \leftarrow 1/(1 + \mathrm{Exp}(-S))$
5: $r \leftarrow 0.1\,(1-Y^2)\cdot(\text{Real part}\,[i]-Y)$
6: $w_1 \leftarrow w_1 - r \cdot C[i]$
7: $w_2 \leftarrow w_2 - r \cdot f[i]$
8: **end for** 9: **return** $s0$

As illustrated in Fig. 12, the predicted value of model output has little difference with the actual value, and the overall error is about 10%. Among them, the error of the real part is relatively large, and the error of the maximum error point is close to 35%. This is because the fatigue loading under the condition of low stress has little influence on the mechanical properties of rock, and the fitting degree of the established complex plane model itself is low. However, the overall error of the real part is about 12%, although the accuracy is not too high, it still has guiding significance to show the changing trend of rock mechanical properties. The error of imaginary part is relatively small, and the overall error is less than 10%, indicating that the model has higher accuracy in predicting rockburst characteristics. By using the established neural network model, the input layer variables were continuously processed

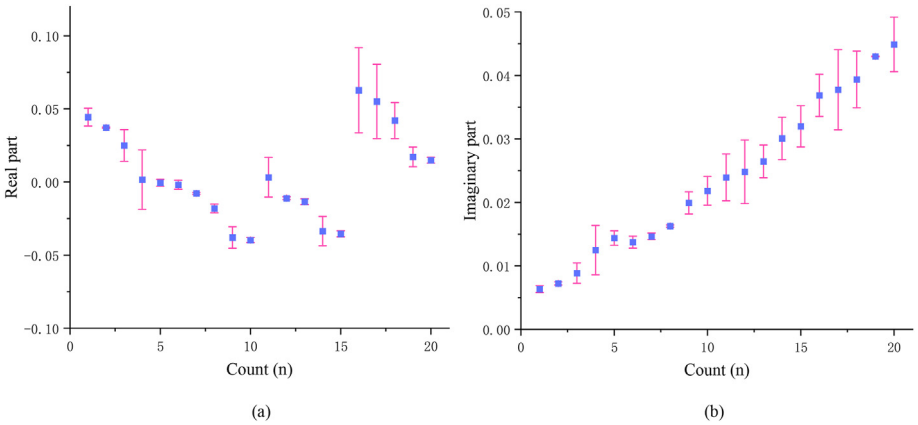

Fig. 12. Error analysis of neural network model. (a) Real part. (b) Imaginary part.

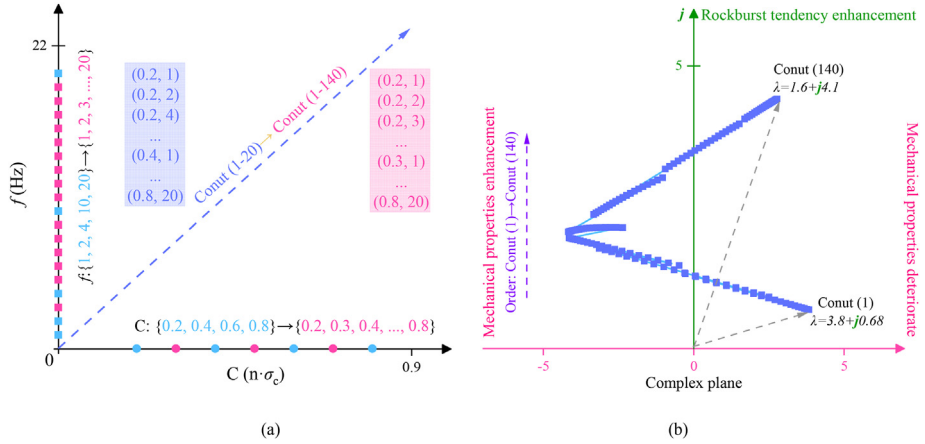

Fig. 13. λ function based on neural network. (a) densified. (b) $\lambda = p + jq$.

(that is, C and f were densified, as shown in Fig. 13(a)), and the neural network model was used for prediction and calculation, and the complex plane image of influence coefficient λ is obtained, as shown in Fig. 13(b).

As can be seen from Fig. 13(b), after continuous processing, the function trend of the model on the complex plane is close to that of the discretized Fig. 10, and their curves have almost the same turning point. The neural network model can input any $\{C, f\}$ values in batches, and calculate the corresponding real part and imaginary part through the built-in model, which greatly improves the practicability of complex plane model.

6. Conclusion

This study employs laboratory testing, theoretical analysis, and model development to investigate the changes in mechanical properties and rockburst characteristics of gypsum-like rock under fatigue loading conditions. The main findings are summarized as follows.

1) The effects of cyclic stress and loading frequency on the mechanical properties and rockburst parameters of the samples are interrelated. The effect of fatigue cyclic stress on the mechanical parameters and rockburst parameters of the samples after fatigue loading is relatively straightforward, while the impact of frequency on the mechanical properties of samples after fatigue loading is more complex. The impact of frequency on mechanical properties and rockburst parameters varies distinctly under different cyclic stress conditions.
2) A degradation index model, expressed as $\{\lambda = p + jq\}$, was developed for samples subjected to fatigue loading. This model calculates both the real and imaginary components and visualizes them on the complex plane. It provides insights into the evolution of rock mechanical properties and rockburst characteristics before and after fatigue loading under varying stress (C) and frequency (f) conditions. The position of the λ curve within the complex plane indicates the overall changes in mechanical properties.
3) To refine and validate the complex plane model, neural network techniques were applied. This approach extends the model by incorporating continuous input factors rather than discrete data points, thereby enhancing the model's practicality and applicability.

CRediT authorship contribution statement

Chongyang Wang: Writing – original draft. **Sijiang Wei:** Methodology. **Dongming Zhang:** Writing – review & editing. **Beichen Yu:** Methodology. **Yisha Pan:** Investigation. **Xunjian Hu:** Software.

Data availability

The datasets generated during and analyzed during the current study are available from the corresponding author on reasonable request.

Funding

Supported by Scientific Research Foundation of State Key Lab of Coal Mine Disaster Dynamics and Control (Project Approval Number: 2011DA105287-zd201804) and National Natural Science Foundation of China (No. 51974104).

Declaration of competing interest

The authors declare that they have no known competing financial interests or personal relationships that could have appeared to influence the work reported in this paper.

References

Arora, K., Chakraborty, T., Rao, K., 2019. Experimental study on stiffness degradation of rock under uniaxial cyclic sinusoidal compression loading. Rock Mech. Rock Eng. 52, 4785–4797. https://doi.org/10.1007/s00603-019-01835-3.

Das, S., Basudhar, P., 2008. Prediction of residual friction angle of clays using artificial neural network. Eng. Geol. 100 (3–4), 142–145. https://doi.org/10.1016/j.enggeo.2008.03.001.

Erarslan, N., Williams, D., 2012. The damage mechanism of rock fatigue and its relationship to the fracture toughness of rocks. Int. J. Rock Mech. Min. Sci. 56, 15–26. https://doi.org/10.1016/j.ijrmms.2012.07.015.

Fan, J., Jiang, D., Liu, W., Wu, F., Chen, J., Daemen, J., 2019. Discontinuous fatigue of salt rock with low-stress intervals. Int. J. Rock Mech. Min. Sci. 115, 77–86. https://doi.org/10.1016/j.ijrmms.2019.01.013.

Haghgouei, H., Baghbanan, A., Hashemolhosseini, H., 2018. Fatigue life prediction of rocks based on a new bi-linear damage model. Int. J. Rock Mech. Min. Sci. 106, 20–29. https://doi.org/10.1016/j.ijrmms.2018.04.009.

Haghgouei, H., Baghbanan, A., Hashemolhosseini, H., Jamali, S., 2021. Variable amplitude fatigue life prediction of rock samples under completely reversed loading. Geotech. Geol. Eng. 39, 1951–1962. https://doi.org/10.1007/s10706-020-01597-8.

He, M., Li, N., Zhu, C., Chen, Y., Wu, H., 2019. Experimental investigation and damage modeling of salt rock subjected to fatigue loading. Int. J. Rock Mech. Min. Sci. 114, 17–23. https://doi.org/10.1016/j.ijrmms.2018.12.015.

Hu, X., Shentu, J., Xie, N., Huang, Y., Lei, G., Hu, H., Guo, P., Gong, X., 2022. Predicting triaxial compressive strength of high-temperature treated rock using machine learning techniques. J. Rock Mech. Geotech. Eng. https://doi.org/10.1016/j.jrmge.2022.10.014.

Hu, X., Liao, D., Ma, D., Xie, S., Xie, N., Hu, H., Gong, X., 2023. Machine learning models for predicting rock fracture toughness at different temperature conditions. Case Stud. Constr. Mater. https://doi.org/10.1016/j.cscm.2023.e02622.

Ishizuka, Y., Abe, T., 1990. Fatigue behaviour of granite under cyclic loading. Static and Dynamic Considerations in Rock Engineering. A. A. Balkema, Rotterdam, pp. 139–147.

Jiang, Y., 2003. Fatigue Failure and Deformation Development Law of Rock under Cyclic Load [M. S. Thesis]. Shanghai Jiaotong University, Shanghai.
Khaledi, K., Mahmoudi, E., Datcheva, M., Schanz, T., 2016. Stability and serviceability of underground energy storage caverns in rock salt subjected to mechanical cyclic loading. Int. J. Rock Mech. Min. Sci. 86, 115–131. https://doi.org/10.1016/j.ijrmms.2016.04.010.
Li, C., Gao, C., Xie, H., Li, N., 2020a. Experimental investigation of anisotropic fatigue characteristics of shale under uniaxial cyclic loading. Int. J. Rock Mech. Min. Sci. 130. https://doi.org/10.1016/j.ijrmms.2020.104314.
Li, N., Chen, W., Zhang, P., et al., 2001. The mechanical properties and a fatigue-damage model for jointed rock masses subjected to dynamic cyclical loading. Int. J. Rock Mech. Min. Sci. 38 (7). https://doi.org/10.1016/S1365-1609(01)00058-2.
Li, T., Pei, X., Guo, J., Meng, M., Huang, R., 2020b. An energy-based fatigue damage model for sandstone subjected to cyclic loading. Rock Mech. Rock Eng. 53 (11), 5069–5079. https://doi.org/10.1007/s00603-020-02209-w.
Liu, Y., Dai, F., Dong, L., Xu, N., Feng, P., 2018. Experimental investigation on the fatigue mechanical properties of intermittently jointed rock models under cyclic uniaxial compression with different loading parameters. Rock Mech. Rock Eng. 51, 47–68. https://doi.org/10.1007/s00603-017-1327-7.
Liu, Y., Dai, F., 2021. A review of experimental and theoretical research on the deformation and failure behavior of rocks subjected to cyclic loading. J. Rock Mech. Geotech. Eng. 13 (5), 1203–1230. https://doi.org/10.1016/j.jrmge.2021.03.012.
Miao, S., Pan, P., Konicek, P., Yu, P., Liu, K., 2021. Rock damage and fracturing induced by high static stress and slightly dynamic disturbance with acoustic emission and digital image correlation techniques. J. Rock Mech. Geotech. Eng. 13 (5), 1002–1019. https://doi.org/10.1016/j.jrmge.2021.05.001.
Momeni, A., Karakus, M., Khanlari, G., Heidari, M., 2015. Effects of cyclic loading on the mechanical properties of a granite. Int. J. Rock Mech. Min. Sci. 77, 89–96. https://doi.org/10.1016/j.ijrmms.2015.03.029.
Nejati, H., Ghazvinian, A., 2014. Brittleness effect on rock fatigue damage evolution. Rock Mech. Rock Eng. 47, 1839–1848. https://doi.org/10.1007/s00603-013-0486-4.
Pan, Y., Wang, C., Wang, Y., 2022. Mechanical degradation mechanism of rock under seismic disturbance stress. Q. J. Eng. Geol. Hydrogeol. 55. https://doi.org/10.1144/qjegh2022-007.
Sang, G., Liu, S., Elsworth, D., 2020. Quantifying fatigue-damage and failure-precursors using ultrasonic coda wave interferometry-sciencedirect. Int. J. Rock Mech. Min. Sci. 131. https://doi.org/10.1016/j.ijrmms.2020.104366.
Song, Z., Konietzky, H., Wu, Y., Du, K., Cai, X., 2022. Mechanical behaviour of medium-grained sandstones exposed to differential cyclic loading with distinct loading and unloading rates. J. Rock Mech. Geotech. Eng. 14 (6), 1849–1871. https://doi.org/10.1016/j.jrmge.2021.12.027.
Sun, B., Zhu, Z., Shi, C., Luo, Z., 2017. Dynamic mechanical behavior and fatigue damage evolution of sandstone under cyclic loading. Int. J. Rock Mech. Min. Sci. 94, 82–89. https://doi.org/10.1016/j.ijrmms.2017.03.003.
Tang, L., Cheng, L., Wang, C., Shu, J., Wu, J., Chen, Y., 2016. Dynamic characteristics of serpentinite under condition of high static load and frequent dynamic disturbance. Rock Soil Mech. 37 (10), 2737–2745. https://doi.org/10.16285/j.rsm.2016.10.001.
Vaneghi, R., Ferdosi, B., Okoth, A., Kuek, B., 2018. Strength degradation of sandstone and granodiorite under uniaxial cyclic loading. J. Rock Mech. Geotech. Eng. 10 (1), 117–126. https://doi.org/10.1016/j.jrmge.2017.09.005.
Wang, C., 2021. Study on Low-Frequency Dynamic Physico-Mechanical Properties of Gypsum Rocks. Henan Polytechnic University, pp. 8–9. https://doi.org/10.27116/d.cnki.gjzgc.2021.000243. MSc Thesis.
Wang, C., Wei, S., Pan, Y., Zhang, S., 2022a. Experimental study on fatigue life of gypsum-like rock under uniaxial compression with different loading frequencies. Pure Appl. Geophys. https://doi.org/10.1007/s00024-022-02966-5.
Wang, C., Wei, S., Wang, M., Xu, C., Zhang, S., 2022b. Rockburst characteristics of gypsum-like rocks after fatigue cyclic loading. Arabian J. Geosci. 15 (15). https://doi.org/10.1007/s12517-022-10636-y.
Wang, C., Wei, S., Zhang, D., Yang, Y., Yu, B., Pan, Y., 2023. Physical properties and tensile strength evolution of gypsum materials under different water content conditions. Construct. Build. Mater. 2023, 364. https://doi.org/10.1016/j.conbuildmat.
Wang, Y., Feng, W., Hu, R., Li, C., 2021. Fracture evolution and energy characteristics during marble failure under triaxial fatigue cyclic and confining pressure unloading (fc-cpu) conditions. Rock Mech. Rock Eng. 54, 799–818. https://doi.org/10.1007/s00603-020-02299-6.
Wei, S., Wang, C., Yang, Y., Wang, M., 2020. Physical and mechanical properties of gypsum-like rock materials. Adv. Civ. Eng. (1), 1–17. https://doi.org/10.1155/2020/3703706.
Xu, T., Fu, M., Yang, S., Heap, M., Zhou, G., 2021. A numerical meso-scale elasto-plastic damage model for modeling the deformation and fracturing of sandstone under cyclic loading. Rock Mech. Rock Eng. 54, 4569–4591. https://doi.org/10.1007/s00603-021-02556-2.
Xu, H., Qi, L., Liu, B., Bai, Z., 2018. Study on poyhting-thomson model of rock salt under cyclic loading. J. Vib. Shock 37 (13), 203–209. https://doi.org/10.13465/j.cnki.jvs.2018.13.032.
Zhang, Q., Liu, Y., Dai, F., Jiang, R., 2022a. Experimental assessment on the fatigue mechanical properties and fracturing mechanism of sandstone exposed to freeze-thaw treatment and cyclic uniaxial compression. Eng. Geol. 306, 106724. https://doi.org/10.1016/j.enggeo.2022.106724.
Zhang, Q., Wang, J., Song, Z., Feng, S., Zhang, Y., Zeng, T., 2022b. Microstructure variation and empirical fatigue model of salt rock under cyclic loading. Rock Soil Mech. 43 (8), 995–1008. https://doi.org/10.16285/j.rsm.2021.1356.
Zhao, K., Ma, H., Yang, C., Chen, X., Liu, Y., Liang, X., Cai, R., 2021. Damage evolution and deformation of rock salt under creep-fatigue loading. Rock Mech. Rock Eng. 54 (4), 1985–1997. https://doi.org/10.1007/s00603-020-02342-6.
Zhao, K., Qiao, C., Luo, F., Hao, Z., 2014. Limestone fatigue property under different frequency cyclic loading test study. Chin. J. Rock Mech. Eng. (S2), 3466–3475. https://doi.org/10.13722/j.cnki.jrme.2014.s2.010.
Zhu, Y., Huang, X., Liu, Y., Liu, Z., Lan, H., Tian, W., 2021. Nonlinear viscoelastoplastic fatigue model for natural gypsum rock subjected to various cyclic loading conditions. Int. J. GeoMech. 21 (5). https://doi.org/10.1061/(ASCE)GM.1943-5622.0001982.